Comprehensive analysis of steady-state and dynamic interactions between Kalman filter-based GFLI and Droop/VSM-based GFMI in conventional

Citation for the original published paper (version of record):
Barua, P., Agneholm, E., Kumar, Y. et al (2026). Comprehensive analysis of steady-state and dynamic interactions between Kalman filter-based
GFLI and Droop/VSM-based GFMI in conventional and fully Inverter-interfaced power systems. Franklin Open, 17. http://dx.doi.org/10.1016/j.fraope.2026.100749

Franklin Open 17 (2026) 100749

Contents lists available at ScienceDirect

Franklin Open

journal homepage: www.elsevier.com/locate/fraope

Comprehensive analysis of steady-state and dynamic interactions between Kalman filter-based GFLI and Droop/VSM-based GFMI in conventional and fully Inverter-interfaced power systems

Pollen Barua [a,b,*], Evert Agneholm [a,b], Yaksh Kumar [a,b], Naime Ahmadi [d], Kjetil Obstfelder Uhlen [c]

[a] *Department of Electrical Engineering, Chalmers University of Technology, Gothenburg, 412 96, Sweden*
[b] *Department of Electrical Engineering, University West, Trollhättan, 461 30, Sweden*
[c] *Department of Electric Energy, Norwegian University of Science and Technology, Trondheim, 7034, Norway*
[d] *Department of Electrical and Computer Engineering, Aarhus University, Aarhus, N 8200, Denmark*

ARTICLE INFO

Keywords:
GFL
GFM
Kalman filter
PLL
SM
100% RES

ABSTRACT

The global energy transition toward renewable sources is driving a shift from conventional synchronous-machine-dominated grids to inverter-based power systems. This necessitates the integration of grid-following (GFL) and grid-forming (GFM) inverters, each with distinct characteristics. As future power systems are expected to include a high share of inverter-based resources, understanding the steady-state and dynamic interactions between GFL, GFM, and synchronous-machine-based grids is important for reliable operation. This research investigates steady-state and transient responses in several prospective scenarios of future power systems. For GFL inverters, a Kalman Filter-based Phase Locked Loop (PLL) is adopted to improve performance under weak-grid conditions, while GFM inverters are modeled using established droop and Virtual Synchronous Machine (VSM) controllers. The study employs inverter capacities from 2.5 MVA to 10 MVA and synchronous machines from 2.5 MVA to 200 MVA to represent different grid conditions. MATLAB/Simulink is used to investigate the interactions between grid-GFL, grid-GFM, and GFL-GFM systems under steady-state small disturbances and transient bolted symmetrical faults. The findings show that the Kalman Filter-based PLL improves the GFL inverter response against transient disturbances compared with a conventional PID-based PLL, particularly in terms of reduced short-circuit current and faster settling. The results also indicate that GFL-GFM interaction can operate stably within the studied 100% renewable-energy-based scenario. For GFMI-SM operation, the results show that stability is strongly affected by the network X/R ratio, and virtual impedance compensation can improve stability under low-X/R conditions within specific limits. In addition to the time-domain study, eigenvalue analysis of the state-space models of both GFM and GFL inverters is carried out to support the observed stability trends. The paper provides a comparative simulation-based assessment of inverter-grid interactions relevant to future renewable-rich power systems.

1. Introduction

Demand for and interest in Renewable Energy Sources (RES) have increased during the last few decades. Global energy production from renewable sources is expected to rise from 30% in 2022 to 76% in 2050, accounting for almost half of all power production, according to the International Energy Outlook [1]. By 2050, the US will produce 80% of its power from renewable energy sources (RES), as indicated by the country's increasing trend toward RES adoption and its ability to sustain hourly supply-demand dynamics. This projection comes from NREL. The EU accelerated its shift away from fossil fuels in 2023, a year with record-low emissions from gas, coal, and other sources. Fossil fuels, which suffered a record 19% decrease to their lowest point ever, account for less than one-third of the electricity generated in the EU [2]. Inverter-based resources (IBRs) are progressively supplanting conventional synchronous machines. In contrast to Renewable Energy Systems (RES), Synchronous Machines are well-established for the current power system and provide inertia and reactive power against any changes, as

* Corresponding author.
E-mail addresses: pollen@chalmers.se, pollen.barua@hv.se (P. Barua).

https://doi.org/10.1016/j.fraope.2026.100749
Received 15 June 2025; Received in revised form 14 July 2026; Accepted 18 August 2026
Available online 19 August 2026
2773-1863/

well as most ancillary services without the need for extra accessories [3,4]. There is a thorough discussion of SM's reactive power support and inertia impact on the conventional grid in [5,6]. Because of decremental percentage of SMs, the existing system is losing its potential to maintain fault current support, steady and dynamic stability, black start capability, reactive power support which maintains a healthy voltage, and inertia which keeps the frequency firm. Additionally, the system's SMs guarantee a high Short Circuit Ratio (SCR), protecting it from disruptions [7]. The current author has conducted a thorough analysis of the impact of RES on power system stability in [8–12]. Large proportions of renewable energy make the grid more prone to system dynamics and failures. As RES involvement rises, power system stability will sharply decrease, with the effects being most severe in island mode. The cause is clearly indicated in [13] in terms of the fault's location and the lack of reactive and kinetic energy throughout the event.

GFL and GFM are the two forms of Inverter Based Resources (IBR) that are most frequently used in power systems. GFL is currently a commonly used IBR. It has already been extensively practiced and materialized for wind and solar energy integration into power grids because of their mature PLL technology, straightforward control structure, and ability to operate at a fixed current (which matches the dispatch point of the resource). GFL converters cannot provide the same inertia as synchronous generators since they typically run at their set output power and do not correspond to fast frequency or voltage changes in the grids . However, the PLL has a negative impact on system stability, especially when the grid becomes weak due to a high grid impedance [14,15]. The Kalman Filter based on prediction, correction, and easily adjustable gain, a robust PLL [16] is developed to test the robustness of PLL against weak or high impedance grids since this paper clearly identifies the PLL problem. The PID-PLL cannot monitor frequency ramps with zero steady-state error and responds to previous accumulated errors, resulting in lag and overrun during abrupt grid changes.

The robustness of the Kalman Filter-based PLL Steady State Linear Kalman Filter -3 (SSLKF-3) is assessed by contrasting its output with that of a linear controller, such as PID, which depends on accumulated phase error. Whereas SSLKF-3 is based on angle, frequency and acceleration state prediction. Rather than reacting to past errors, SSLKF-3 models the physics of the grid signal and predicts where the angle will be. To monitor the behavior of the entire power system, the GFL is then fused with a weak grid and in a 100% RES based power system case.

When SM is absent, one or some inverters in a system powered entirely by renewable energy should jump from "grid-following" to "grid-forming" operation. By generating voltage and frequency references for additional inverter-based generators, these Grid Forming (GFM) inverters reduce the requirement for a rigid voltage source and preserve stable grid functioning [17]. To manipulate the grid voltage and frequency in a system that is 100% inverter-based, GFM inverters are considered an essential part of the power system [18–20]. Primary frequency regulation is a capability of GFM inverters that has been proven to be absent from GFL inverters [21,22]. To ensure reliable operation, a GFM inverter requires a dispatchable energy supply. Since many RESs are non-dispatchable, the GFM inverter typically needs to be used in conjunction with an Energy Storage System (ESS) [23,24]. The location and size of the GFM inverter will affect its capacity to control voltage and frequency [25]. Droop-based and synchronous machine-based GFM control techniques are categorized very separately and assigned to the principal control loop [26]. In addition, virtual impedance loop, voltage, and current are required for GFM modeling [27]. This present work uses virtual synchronous machines (VSM) and droop-based control techniques to execute various case scenarios of operating SM and inverters in parallel.

To demonstrate stability of the system both time domain and Eigenvalue based study are carried out in this paper. It is possible to apply the state-space technique to any linearized system. All the eigenvalues for the stability analysis may be computed using the state-space matrix, allowing for an accurate prediction of the system's stability boundary [28]. Nevertheless, it requires a thorough understanding of the system's control design, which is frequently challenging to acquire and validate in actual use [29]. It is therefore only appropriate for the white-box system.

The purpose of this paper is to provide a system-level evaluation of how grid-following inverters, grid-forming inverters, and synchronous machines interact in the power systems of the energy transition — from today's SM-dominated grids to fully inverter-based networks. Rather than proposing new control structures, this work adopts established building blocks from the literature — the SSLKF-3 Kalman filter-based PLL [16,37,38], which has been shown to be mathematically equivalent to enhanced SRF-PLL structures [37], and standard droop/VSM-based grid-forming control — and subjects them to conditions not examined in their original developments. Specifically, the paper contributes: (i) transient fault analysis of the SSLKF-3 PLL, which prior works implemented and verified but did not evaluate under bolted-fault, multi-machine conditions; (ii) a structured investigation of multiple interaction configurations — grid–GFL, grid–GFM, GFL–GFM in a 100% RES network, and GFM–SM under weak- and strong-grid conditions — within a unified time-domain and eigenvalue framework; and (iii) a characterization of the network- and machine-dependent conditions governing GFM–SM transient stability, together with the applicability limits of virtual impedance as a control-based mitigation. Table 1 positions these contributions against the most closely related prior works.

2. GFL and GFM inverter

As the usage of RES increases, the electric power system will experience a change in perspective. RESs and existing power systems are communed via inverters. These inverters are commonly divided as either grid-forming (GFMI) or grid-following (GFLI) inverters based on their working principle and control. GFLI can manipulate their power output by using a phase-locked loop (PLL) to measure the grid voltage angle [30,31]. As a result, GFLI harmonizes with the grid and operates as a supervised current source [32]. They just track the defined grid angle and frequency of the utility networks. Inverter controllers typically employ droop control to confirm appropriate power coordination across many generators. GFL inverters determine the active and reactive power based on their individual droop characteristics using the system frequency reference and grid voltage provided by the PLL. GFL inverters determine the active and reactive power based on their individual droop characteristics using the system frequency reference and grid voltage provided by the PLL.

In contrast, grid-forming source (GFM) voluntarily regulates the output voltage and frequency and is widely utilized in microgrid setup. A controlled voltage source linked in series with an equivalent impedance can be used to simulate a grid-forming inverter. GFMIs reduce the effect of mechanical inertia on frequency dynamics by offering active frequency management. Thus, GFMIs can support grid stabilization. GFMI, as an counter to GFLIs, employ measured power as input and droop to keep the grid voltage and frequency steady. The inverter controller is described by a spinning direct-quadrature (dq) frame, sometimes called a synchronous reference frame [33]. The inverter controller is depicted in Fig. 1; depending on the circumstance, it can operate in grid-forming or grid-following modes. Using two cascaded PI controllers, the controller creates voltage and current references in the

Table 1
Positioning of this paper's contributions relative to closely related prior works.

Ref.(s)	Focus of Earlier Work	Remaining Gap	Contribution of This Paper
[14,15]	Comparative reviews of grid-following (GFL) and grid-forming (GFM) control strategies, covering control structure, stability, and application challenges.	These are review/comparative studies of control principles; they do not investigate the dynamic interactions among GFL, GFM, and SM under a unified simulation framework.	This paper investigates multiple interaction combinations — grid–GFL, grid–GFM, GFL–GFM, and GFM–SM — within a single simulation framework, under both steady-state disturbances and bolted symmetrical faults.
[16,38]	Development and implementation of Kalman-filter-based grid synchronization (PLL) techniques, including the underlying SSLKF-type algorithm.	These works establish and implement the PLL algorithm itself but do not subject it to fault analysis or examine its behavior within multi-machine interaction studies.	This paper adopts the SSLKF-3 PLL and investigates its performance under bolted fault conditions and weak-grid operation, evaluating its influence on GFL response and on GFL–GFM interaction — an operating regime not examined in the original implementations.
[37]	Demonstrates that steady-state linear Kalman-filter-based PLLs (SSLKF-PLLs) are mathematically equivalent to established enhanced SRF-PLL structures, with implementation-level verification.	The analysis addresses the PLL structure in isolation; no transient fault analysis or system-level interaction study involving synchronous machines or grid-forming inverters is performed.	This paper acknowledges the structural equivalence and, going beyond implementation, subjects the SSLKF-3 PLL to transient fault analysis within GFL–SM and GFL–GFM configurations, evaluating synchronization recovery, current stress, and interaction behavior.
[27]	Comparative study of GFM control strategies (including droop and VSM) in the frequency and time domains.	Establishes and compares GFM control principles in isolation; does not examine GFM interaction with synchronous machines of differing strengths, nor the network-parameter dependence of transient stability.	This paper uses established droop/VSM-based GFM models to study transient GFM–SM interaction across weak- and strong-grid configurations, identifying the network and machine conditions that govern stability.
[28,29]	Impedance compensation and impedance-based circuit interpretation of grid-forming inverter control, including extending stability range in weak grids.	The general principle of impedance compensation is established, but its applicability limits under fault conditions, and its dependence on network parameters and machine inertia, are not characterized.	This paper evaluates virtual impedance as a fault-time mitigation within GFM–SM interaction studies, characterizing the conditions under which it is effective and identifying the mechanisms that bound its applicability.
[34]	Direct comparison of droop-based GFM and PLL-based GFL control during a symmetrical fault.	Compares GFM and GFL fault responses in isolation; does not consider an SSLKF-type PLL, GFM–SM interaction across grid strengths, or mitigation strategies for adverse network conditions.	This paper extends the comparison to SSLKF-3-based GFL behavior, GFL–GFM cooperation in a 100% RES scenario, and GFM–SM interaction under both weak- and strong-grid conditions, including mitigation via virtual impedance.
This paper	The building blocks (SSLKF-3, droop, VSM, virtual impedance) are adopted from established literature; the contribution lies in their comparative, system-level evaluation. Specifically: (i) transient fault analysis of the SSLKF-3 PLL, which prior works implemented but did not subject to fault studies; (ii) a structured investigation of multiple interaction configurations — grid–GFL, grid–GFM, GFL–GFM in a 100% RES network, and GFM–SM in weak and strong grids — under a unified time-domain and eigenvalue framework; and (iii) characterization of the network- and machine-dependent conditions governing GFM–SM transient stability, together with the applicability limits of virtual impedance as a control-based mitigation.		

dq-frame. When the inverter is operating in GFL mode, it regulates the quantity of active and reactive power sent to the main grid. PLL uses the grid voltage as an input to determine the frequency set point when a system is in operation with the grid.

3. Voltage control loop

The prime job of the regulator of voltage in Fig. 2 (described in appendix) is to control the voltage across the capacitor Cf. When modeling the voltage controller, the resistor is disregarded because the reactance of the capacitor at 50 Hz is larger than that of the damping resistor R_d. Kirchhoff's law is implemented to the electrical circuit shown in Fig. 2. The current i_i flows through inverter is given by Eq. (1) if R_d is small value.

$$i_i = i_o + C_f * \frac{dV_g}{dt} \tag{1}$$

transforming (2) into d-q frame, (3) is determined.

$$C_f\frac{dv_g^d}{dt} - \omega C_f v_g^q = i_i^d - i_0^d \tag{2}$$

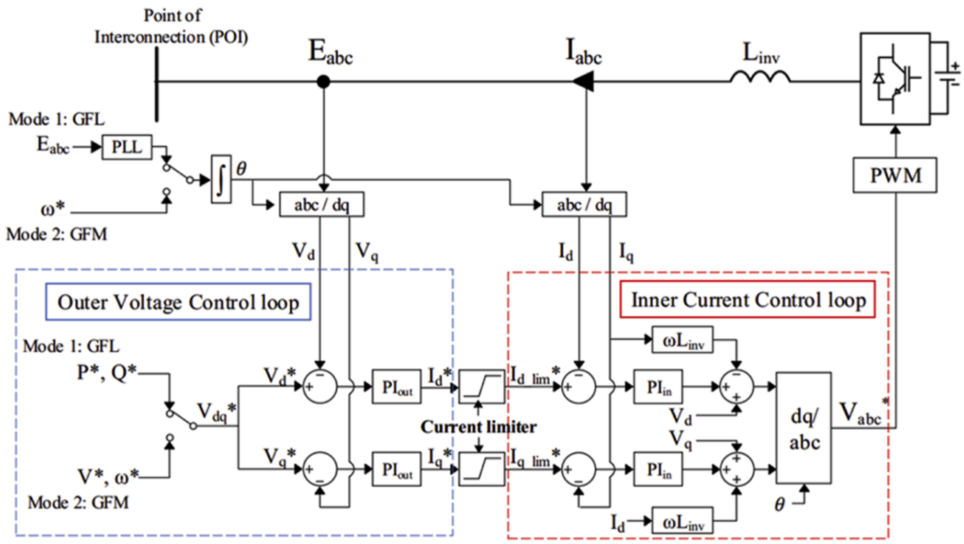

Fig. 1. Inner and outer control loop in dq-frame [34].

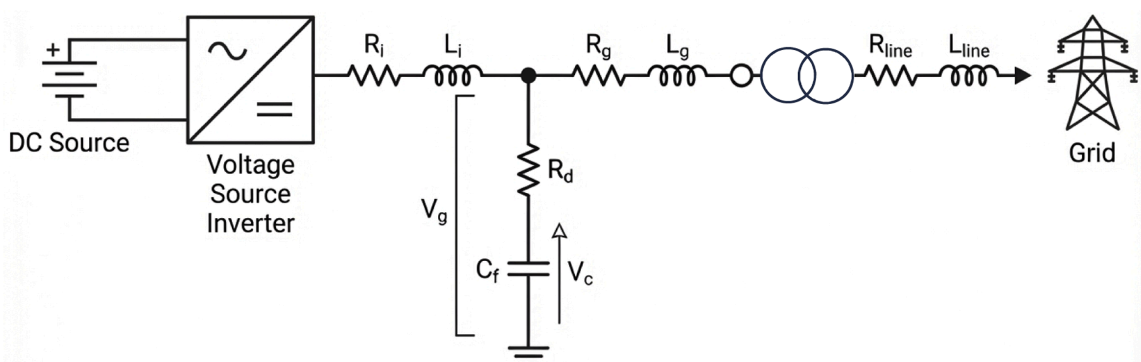

Fig. 2. IBR and grid interfacing circuit.

$$C_f \frac{dv_g^q}{dt} + \omega C_f v_g^d = i_i^q - i_0^q \tag{3}$$

After Laplace transformation (3) takes the form of (4)

$$\begin{aligned} v_g^d &= \left(i_i^d - i_0^d + \omega C_f v_g^q\right)\frac{1}{sC_f} \\ v_g^q &= \left(i_i^q - i_0^q - \omega C_f v_g^d\right)\frac{1}{sC_f} \end{aligned} \tag{4}$$

$\omega C_f v_g^{q/d}$ is eliminated by a feed-forward term to enhance the dynamic response of the controller and the association between the equations. By doing this, a PI-controller represented in Eq. (5) open loop transfer function can adjust the voltage. The proportional and integral gains of the PI voltage regulator are denoted here by K_{pv} and K_{iv}.

$$H_{OL,s}(s) = H_{PI,v}(s) H_{sys,v}(s) = \left(K_{pv} + \frac{K_{iv}}{s}\right)\frac{\frac{1}{C_f}}{s} \tag{5}$$

The equation that results from combining Eqs. (3) and (5) is Eq. (6). This is the voltage controller's modeling equation. The voltage controller's output, which is the inner current controller's reference, is located on the left side of the equation.

$$\begin{aligned} i_{ref}^d &= i_0^d + \left(v_{c,ref}^d - v_g^d\right)\left(K_{pv} + \frac{K_{iv}}{s}\right) - v_g^q \omega * C_f \\ i_{ref}^q &= i_0^q + \left(v_{c,ref}^q - v_g^q\right)\left(K_{pv} + \frac{K_{iv}}{s}\right) + v_g^d \omega * C_f \end{aligned} \tag{6}$$

4. Current control loop

The prime intention of the current regulator is to tune the current that is seen by the inverter side inductor. This responds to the present i_i shown in Fig. 2. The formation of the present controller uses dq-frame to simplify the modeling process. By initially applying Kirchoff's voltage law to the LCL-filter in the electrical circuit depicted in Fig. 2, Eq. (7) is generated. The resulting voltage of the VSC appears here by V_i.

$$v_i = R_c i_i + L_c \frac{d}{dt}\left(i_i^d + j i_i^q\right) + v_g \tag{7}$$

Transforming (7) will yield coupling equation as (8)

$$\begin{aligned} L_c \frac{di_i^d}{dt} - \omega L_c i_i^q &= v_i^d - R_c i_i^d - v_g^d \\ L_c \frac{di_i^q}{dt} + \omega L_c i_i^d &= v_i^q - R_c i_i^q - v_g^q \end{aligned} \tag{8}$$

Eq. (9) is eventually achieved by applying Laplace's Transformation to transform into the frequency domain and dividing by the inductance.

$$\begin{aligned} i_i^d &= \left(v_i^d - v_g^d + \omega L_c i_i^q\right)\frac{\frac{1}{L_c}}{s+\frac{R_c}{L_c}} \\ i_i^q &= \left(v_i^q - v_g^q + \omega L_c i_i^d\right)\frac{\frac{1}{L_c}}{s+\frac{R_c}{L_c}} \end{aligned} \tag{9}$$

Regarding the voltage controller, $\omega L_c i_i^{d/q}$ connects the two axes. A feed-forward coupling discards them and allows for a quicker response. Furthermore, a PI-controller operating on the open loop transfer function represented in Eq. (10) can be used to control the current. Here, the PI current tuning proportional and integral gains are shown by $K_{p,c}$ and $K_{i,c}$, orderly.

$$H_{OL,c}(s) = H_{PI,c}(s)H_{sys,c} = \left(K_{p,c} + \frac{K_{i,c}}{s}\right)\frac{\frac{1}{L_c}}{s+\frac{R_c}{L_c}} \tag{10}$$

Mixing up (8) and (10), deliver the reference signal for VSC as (11).

$$\begin{aligned} v_{ref}^d &= v_c^d + \left(i_{ref}^d - i_i^d\right)\left(K_{p,c} + \frac{K_{i,c}}{s}\right) - \omega L_c i_i^q \\ v_{ref}^q &= v_c^q + \left(i_{ref}^q - i_i^q\right)\left(K_{p,c} + \frac{K_{i,c}}{s}\right) + \omega L_c i_i^d \end{aligned} \tag{11}$$

5. Phase lock loop (PLL)

Phase-locked loops (PLLs) are among the most popular techniques for obtaining grid voltage characteristics for energy and power applications, as well as for grid synchronization of power electronics converters. The synchronous reference frame PLL (SRF-PLL) is the most often used PLL structure [35]. Fig. 3 shows the block diagram of a conventional closed loop PLL system. The Phase Detector and Loop Filter in the system produce the grid phase angle estimation $\tilde{\theta}_g$ by utilizing the phase error e. Typically, a loop filter is constructed with an integrator and a proportional integral regulator (PI) that finds out the calculated values of the grid angular frequency $\tilde{\omega}_g$ The loop filter is a proportional-integral (PI) regulator with K_p proportional and K_i integral gain set the phase error signal V_q to zero. The grid voltage frequency is estimated using the loop filter's output signal. The vector product yields the signal error e, which is the difference between the estimated angle $\tilde{\theta}_g$ and the grid voltage phasor angle θ_g. For tiny signals, this approximation formula can be used [36]:

$$\begin{aligned} \mathrm{e} &= \frac{V_\beta Cos\tilde{\theta}_g - V_\alpha Sin\tilde{\theta}_g}{V_S} \\ &= sin\theta_g \,.\, cos\theta_g - cos\theta_g \,.\, sin\theta_g \\ &= sin(\theta_g - \tilde{\theta}_g) \cong (\theta_g - \tilde{\theta}_g) \end{aligned} \tag{12}$$

where V_S is the grid voltage phasor module and V_α and V_β are the horizontal and vertical components of the grid voltage phasor, represented by a stationary reference frame αβ.

The loop filter used in this paper is a deterministic prediction-correction filter, which is built from a SSLKF. Grid-connected applications have already used prediction-correction filters [38], demonstrating their efficacy in estimating phase and frequency even under atypical grid operating scenarios. Due to the PLL system's requirement for implementation in a digital device, the current contribution offers a deterministic filter structure immediately as a prediction model followed by a correction model, both offered in discrete-time form. The SSLKF-PLL blocks are shown in Fig. 4 [37]. Since acceleration, velocity, and angle are anticipated, a significant jump in grid frequency can be taken into consideration, making this a 3-state prediction model.

6. Kalman filter

Assigning the Kalman Filter (KF) is a computationally fruitful way to extrapolate the state of a process that can reduce the squared error mean. This is accomplished by following the variance of the guesses and the forecasted state of the system taking two distinct phases: update and predict. The definition of the basic KF is:

$$\widehat{X}_k = A_k X_{k-1} + W_K$$

The state transition matrix at time k is given by A_k, the projected new condition by $\widehat{X}_k$, the previous estimated state by X_{k-1}, and the state noise transition matrix by W_K. The projected process covariance matrix $\widehat{P}_k$ can be produced on the other hand using the prior covariance P_{k-1} and covariance noise Q_K in the manner described below:

$$\widehat{P}_k = A_k P_{k-1} {A_k}^T + Q_k$$

Kalman gain will be represented as:

$$\widehat{Y}_k = B_k X_{mk} + R_k$$

The state noise transition matrix during gain finding equation is denoted by R_k, the obtained new input is denoted by $\widehat{Y}_k$, the measured state is X_{mk}, and B_k is the state transition matrix at time k. As written below, the foreseen and measured states with process covariance $\widehat{P}_k$ and measurement covariance matrix R are used to find the Kalman filter gain:

$$KG_k = \widehat{P}_k H\left(H_k \widehat{P}_k {H_k}^T + R\right)^{-1}$$

The eventual output of the current iteration, anticipated covariance, and forecast state will be updated using Kalman Gain to predict the subsequent states. The updating procedures are mentioned below [39].

$$X_k = \widehat{X}_k + KG\left(\widehat{Y}_k - H_k \widehat{X}_k\right)$$

$$P_k = (I - KGH_k)\widehat{P}_k$$

The state space model of SSLKF-PLL-3 in this work, which is mentioned in Section 1.3 can be represented as follows:

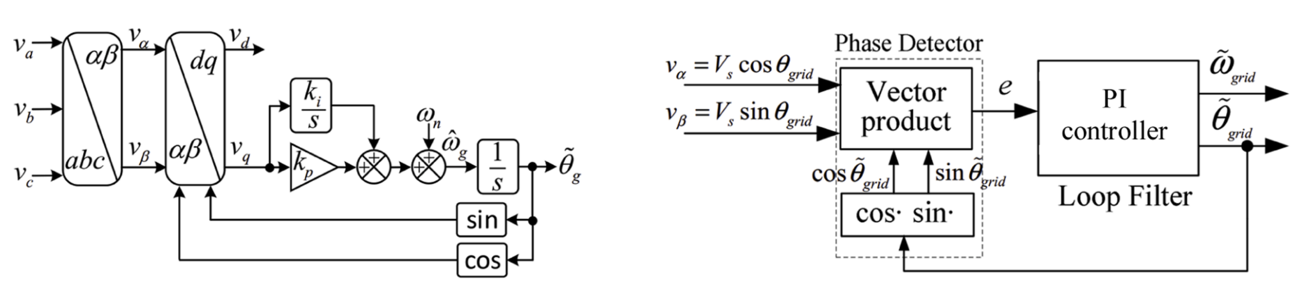

Fig. 3. Block diagram of a classical PLL [37].

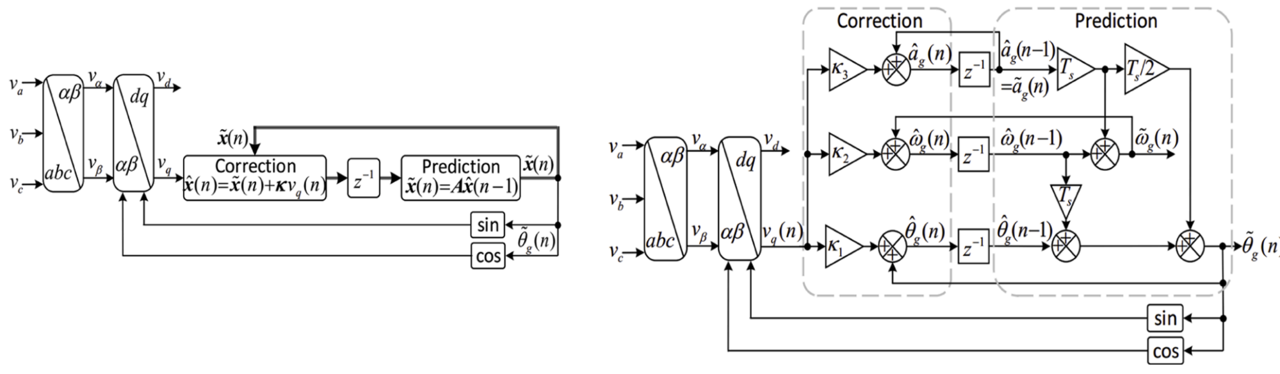

Fig. 4. Block diagram of a SSLKF-PLL-3 state prediction model [37].

$$\begin{aligned}&\mathrm{x(n)}=\mathrm{Ax(n-1)}\\&\mathrm{y(n)}=\mathrm{Cx(n)}\\&\mathrm{x^T}=[\theta_g\omega_g\alpha_g];\\&\mathrm{A}=\left[1\,T_s\,\frac{T_s^2}{2}\;\;;\;0\,1\,T_s\;;\;\;0\,0\,1\right]\\&C=[1\,0\,0]\end{aligned} \tag{13}$$

The grid voltage angle in this case is Θ_g, the angular frequency is ω_g, and the current sample is denoted by n, while the preceding sample is represented by (n-1). The 10 kHz sampling frequency, or $T_s = 0.0001$ s, is considered in this paper. The prediction/correction filter performs the following actions to precisely estimate the state variables based on the model given in (13) as follows at each sample:

a) Prediction: All three states are projected forward one sample using the kinematic transition matrix:

$$\widetilde{\theta}_g(n) = \widehat{\theta}_g(n-1) + \widehat{\omega}_g(n-1)T_s + \frac{1}{2}\widehat{\alpha}_g(n-1)T_s^2$$

$$\widetilde{\omega}_g(n) = \widehat{\omega}_g(n-1) + \widehat{\alpha}_g(n-1)T_s$$

$$\widetilde{\alpha}_g(n) = \widehat{\alpha}_g(n-1)$$

b) Correction: Using the phase error $\theta_e(n) \;= \theta_{grid}(n) - \widetilde{\theta}_g(n)$, all three states are corrected simultaneously:

$$\widehat{\mathbf{x}}(n) = \widetilde{\mathbf{x}}(n) + \mathrm{K}{\cdot}\theta_e(n); \mathrm{KT} \;=\; [\mathrm{K1\ K2\ K3}].$$

$$\widehat{\theta}_g(n) = \widetilde{\theta}_g(n) + K_1{\cdot}\theta_e(n)$$

$$\widehat{\omega}_g(n) = \widetilde{\omega}_g(n) + K_2{\cdot}\theta_e(n)$$

$$\widehat{\alpha}_g(n) = \widetilde{\alpha}_g(n) + K_3{\cdot}\theta_e(n)$$

1) $\tilde{x}(n) = A\hat{x}\,(n-1)$ predicts the states at the subsequent sampling period.
2) Using the phase error information, correct the anticipated states as follows: $\hat{x}\,(n) = \tilde{x}(n) + K^{*}\,\theta_e(n)$; where $K^T = [K_1\ K_2\ K_3]$.
3) In this present work, K^T=[0.9 10 150]

7. Droop control

Droop manipulation techniques are used in grid-dependent power converters to control the trading of active and reactive powers with the grid, hence controlling the frequency and amplitude of the grid voltage. The main idea behind supporting the droop control is to mimic the self-regulation capability of the synchronous generator when it is connected to the grid by lowering the amount of reactive power injected in response to an increase in grid voltage amplitude and lowering the amount of active power delivered in response to an increase in grid frequency. The droop controller coefficients are chosen by measuring the extent of interdependence that P − f and Q − V ought to have. This can only be accomplished by establishing minimum and maximum levels for both the voltage and frequency levels.

$$\begin{aligned}V_{max} &= (1+\Delta V) * V_n\\ V_{\min} &= (1-\Delta V) * V_n\end{aligned} \tag{14}$$

According to (14), the f_{max} and f_{min} can also be obtained. The droop coefficients are then calculated as (15).

$$\begin{aligned}m_q^* &= \frac{V_{max} - V_{min}}{Q_{\mathrm{rated}}}\\ n_p^* &= \frac{\omega_{max} - \omega_{min}}{P_{\mathrm{rated}}}\end{aligned} \tag{15}$$

In droop, the connection of true power and frequency and imaginary power and voltage are as shown in (16),

$$\begin{aligned}\omega - \omega* \quad &= -n_p^*(P - P*)\\ V - V* \quad &= -k_q(Q - Q*)\end{aligned} \tag{16}$$

8. Virtual synchronous generator (VSG) and virtual impedance (VI)

8.1. VSG

GFMIs are categorized into various types based on the configuration of their primary control loops. These varieties include droop and VSG, among others. The VSG based GFMI is covered in this section. Managing

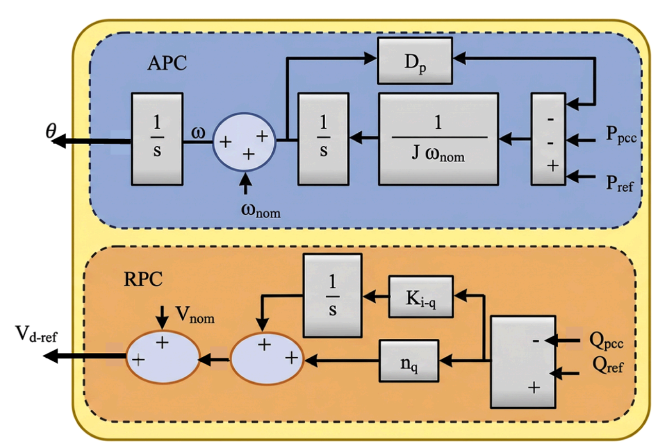

Fig. 5. Primary control loop as VSG.

the injection of reactive power at the common connection, Qpcc at the PCC, and real power at the point of common connection (PCC), as shown in Fig. 5, into the grid in accordance with the desired references The GFMI's primary control objective is Pref and Qref. The reactive power controller (RPC) and the active power controller (APC) are typically utilized in tandem to achieve this control objective. It first uses voltage and current measurements (Vpcc;ipcc) to calculate Ppcc and Qpcc.

Tuning the control parameters within the APC within the VSG framework to meet grid code criteria, considering terms like the RoCoF, takes operational limitation like the rated output power of the GFMI into account. The APC of the VSG control system find out the damping factor (D_p) and the inertia factor (J) as the two regulating parameters. As mentioned in (17.1), the D_p is determined as the opposite of the parameter m_p. J is calculated as indicated in (17.2) if the nominal grid angular frequency (ω_{nom}) is linked to the parameter T_{VSG} and the intended starting RoCoF (e.g., T_{VSG} is within the range of 0.5 to 1 Hz/s as RoCoF, as detailed in references [40] and [41].

$$D_p = \frac{1}{m_p} = \frac{2P_{rated}}{2\pi(f_{max} - f_{min})} \tag{17.1}$$

$$J = T_{VSG}\frac{D_p}{\omega_{nominal}} \tag{17.2}$$

8.2. VI

VI in a grid-forming inverter (GFMI) is implemented by modifying the voltage reference (as shown in Fig. 5) using the measured output current, without adding any physical impedance to the network. In the synchronous *dq* frame, the compensated voltage references are given by,

$$v_{d,\mathrm{VI}*} = v_{d*} - R_v I_d + X_v I_q \tag{18.1}$$

$$v_{q,\mathrm{VI}*} = v_{q*} - R_v I_q - X_v I_d \tag{18.2}$$

where $v_{d,\mathrm{VI}*}$, $v_{q,\mathrm{VI}*}$ are the d and q axis modified reference voltage respectively; R_v and X_v are the virtual resistance and reactance gains; and I_d and I_q are the inverter output currents. The cross-coupling terms associated with X_v emulate the 90° phase shift of a physical inductance, producing a current-dependent voltage drop like that of a series reactor. The compensated references $v_{d,\mathrm{VI}*}$ and $v_{q,\mathrm{VI}*}$ replace the droop-generated voltage references at the input of the voltage-control loop, while the current controller and PWM stage remain unchanged. Consequently, the inverter presents a higher effective X/R ratio to the network, improving active–reactive power decoupling and enhancing stability under low-X/R grid conditions.

9. State space modelling

The differential equations of several parts associated with Fig. 2 are linearized to construct a state matrix. LCL filter, grid, outer and inner loop controllers linearized models are augmented to establish the overall state matrix. These linearized differential equations allow for the formation of the small-signal state-space model. This state matrix is analyzed with Eigenvalue and Eigen vector. Product of state matrix and Eigen vector can be decomposed to Eigenvalue and Eigen vector. Eigenvalues of this state matrix help to determine the stability of the system. Any positive value will cause the entire system to be unstable against small disturbances.

From L-C-L filter circuit corresponding to Fig. 2, the differential equations are:

$$\begin{aligned}
&C_f\frac{dv_g^d}{dt} - \omega C_f v_g^q = i_i^d - i_0^d - \frac{V_g^d}{R_d}\\
&C_f\frac{dv_g^q}{dt} + \omega C_f v_g^d = i_i^q - i_0^q - \frac{V_g^q}{R_d}\\
&L_c\frac{di_i^d}{dt} - \omega L_c i_i^q = v_i^d - R_c i_i^d - v_g^d\\
&L_c\frac{di_i^q}{dt} + \omega L_c i_i^d = v_i^q - R_c i_i^q - v_g^q\\
&L_T\frac{di_0^d}{dt} - \omega L_T i_0^q = v_g^d - R_T i_0^d - v_T^d\\
&L_T\frac{di_0^q}{dt} + \omega L_T i_0^d = v_g^q - R_T i_0^q - v_T^q
\end{aligned} \tag{19}$$

From inner loop controller circuit corresponding to Fig. 1, the differential equations are:

$$\begin{cases} \dfrac{dInt_{id}}{dt} = i_{id}{}^* - i_{id}^{cntrl} \\ v_i^{d*} = K_{p\_id}\left(i_{id}{}^* - i_{id}^{cntrl}\right) + K_{i\_id}\cdot Int_{id} - \omega_N L_c i_{iq}^{cntrl} + V_g^* \end{cases} \tag{20}$$

$$\begin{cases} \dfrac{dInt_{iq}}{dt} = i_{iq}^* - i_{iq}^{cntrl} \\ v_i^{q*} = K_{p\_iq}\left(i_{iq}{}^* - i_{iq}^{cntrl}\right) + K_{i\_iq}\cdot Int_{iq} + \omega_N L_c i_{id}^{cntrl} \end{cases} \tag{21}$$

Here, $\mathrm{Int}_{id/q}$ are the state variables of integrator in d-q axis, $K_{p\_id/iq}$, $K_{i\_id/iq}$ are the proportional and integral gain.

From outer loop controller circuit corresponding to Fig. 1, the differential equations are:

$$\begin{cases} \dfrac{dInt_P}{dt} = P^* - P_{LPF}^{ctrl} \\ i_i^{d*} = K_{p\_P}\left(P^* - P_{LPF}^{ctrl}\right) + K_{i\_P}\cdot Int_P \end{cases} \tag{22}$$

$$\begin{cases} \dfrac{dInt_V}{dt} = V_o^* - V_{oLPF}^{ctrl} \\ i_i^{q*} = K_{p\_V}(-1)\left(V_o^* - V_{oLPF}^{ctrl}\right) + K_{i\_V}(-1)\cdot \mathrm{Int}_V \end{cases} \tag{23}$$

Here, $\mathrm{Int}_{p/v}$ are the state variables of the integrator in power and voltage outer loop, $K_{p\_p/v}$, $K_{i\_p/v}$ are the proportional and integral gain. State variables of the system:

$$\Delta x_{10\times 1} = \left[\ \Delta i_0^d, \Delta i_0^q, \Delta v_g^d, \Delta v_g^q, \Delta i_i^d, \Delta i_i^q, \Delta Int_{id}, \Delta Int_{iq}, \Delta Int_P, \Delta Int_V \right]^{\mathrm{T}} \tag{24}$$

10. Methodology

This paper investigates the parallel operation between VSC and SM based system with loads in steady and transient state. Two types of VSCs are used, they are GFL and GFM. GFL is again used with two types of PLL separately, one is SSLKF-3 and another is PID. SMs are modelled in d-q-0 axis, with IEEE DC type 2 exciter and fundamental Hydro turbine governor [42]. Both weak and strong grids are used in terms of short circuit ratio (SCR) to investigate the system properties against disturbances. To obtain a 100% renewable based power system, it also runs parallel operation between VSCs. These VSCs range from 2.5 MVA to 10 MVA and SMs range from 2.5 MVA to 200 MVA depending on several scenarios. To demonstrate the steady state stability, the step load change is carried out whereas for the transient analysis, the short circuit is applied near and remote bus. State matrix of both GFL and GFM are analyzed to find out the Eigenvalues to exhibit the stability.

11. Result and discussion

GFLI and weak grid. To examine the stability of GFLI, a 2 MW rated GFLI is connected to 1.5 MW, 0.1 MVAR load at 0 s. which is followed by 0.5 MW and 0.1 MVAR step load increment at 5 s. Fig. 6 (a) to (i) show the smoother voltage, current component and power tracking.SSLKF3 exhibits quick response against large disturbances since it considers angular acceleration. Hence, we get smoother response from all red curves compared to blue curves in these plots. To check the transient stability, a 3-phase symmetrical short circuit is applied at 6.5 s. for 4 cycles which has no resistance. Fig. 7 shows the effectiveness of SSLKF3 based PLL in tracking power and faster voltage stability. Different fault responses between the two PLL techniques are shown in Fig. 8. Due to integrator windup from failed phase tracking, PID-PLL continually saturates the ±4000 A hardware limit, causing severe spikes between 6.5–6.7 s. SSLKF3-PLL confirms that its acceleration state actively tracks rapid grid angle dynamics rather than driving limit saturation by constraining I_d between -500 to 3000 A but it is oscillatory as expected due to acceleration state tracking . I_q is also maintained within safe bounds despite sharing similar current controller hardware. As a result, SSLKF3 shows better GFLI performance in weak grids by eliminating integrator windup and achieving around 20 ms. faster post-fault recovery as shown in Fig. 8.

The state matrix of state space model of GFLI inverter is analyzed in terms of Eigen value and Eigen vector. Some critical Eigen values are plotted in Fig. 9, where it is found that critical values are on the left half plane with a damping ratio of 0.72. It reveals that the GFLI is a stable system with an inner and outer loop controller.

GFLI and GFMI. As a second scenario, the 100% RES is modelled. In this system a GFLI and a GFMI inverter each of 10 MVA are chosen but loaded around one fourth of its rating. GFLI is loaded with 2 MW and steps up to 2.5 MW whereas GFMI is step up from 1 MW to 2 MW as shown in Fig. 10. From the frequency plot it is observed that the GFLI is following the frequency of GFMI which forms the grid. Now to monitor the transient stability and better performance of SSLKF3, a 3-phase bolted fault of 4 cycles is applied. Fig. 11 is plotted based on PID-PLL and Fig. 12 using SSLKF3-PLL. SSLKF3 shows far less short circuit and recovery current stress than PID.

GFMI and weak grid. In this scenario a GFMI of 2.5 MVA is connected to a SM which is of same size having frequency droop of 2% each. Before 0.6 *sec*, both the GFMI and SM run individually at 50.025 and 50.005 Hz. At 0.6 s., they are thrown to parallel operation. At 1.4 s. they both attain a busbar frequency which is 50 Hz. They share a common bus bar voltage at 0.65 s. as shown in Fig. 13.

To check the transient stability, a 3-phase bolted symmetrical fault is applied at different X/R ration as indicated in Fig. 14(a). In a small ratio

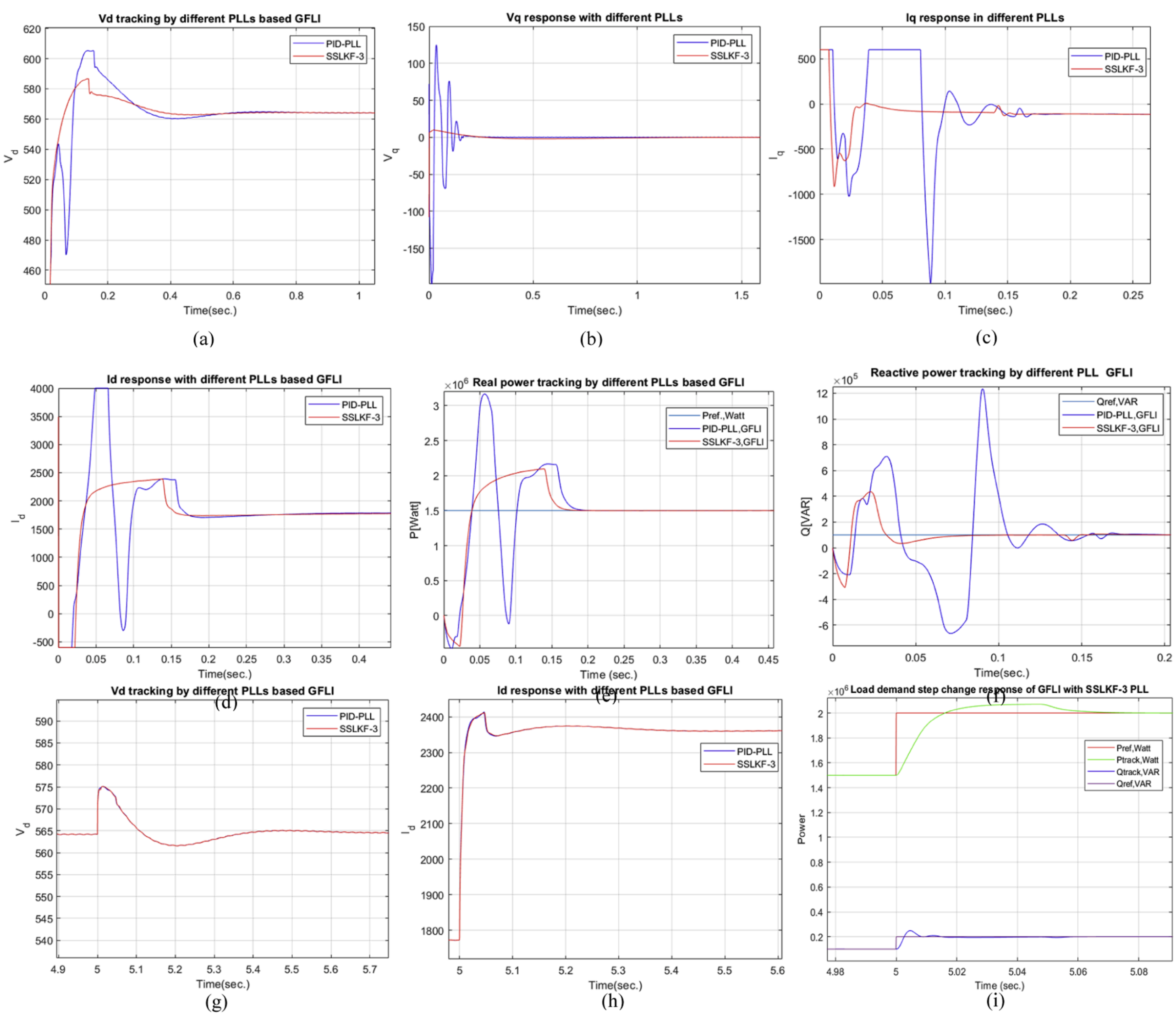

Fig. 6. Components responses of GFLI inverter against step load change.

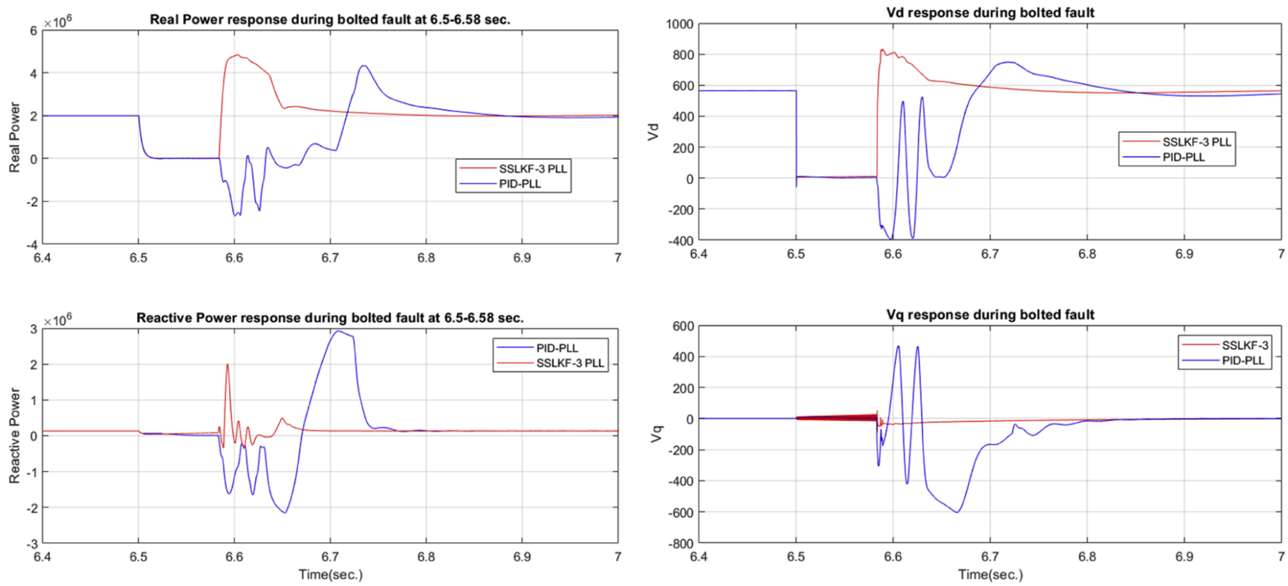

Fig. 7. Power and Voltage response of GFLI inverter against 3-phase symmetrical fault.

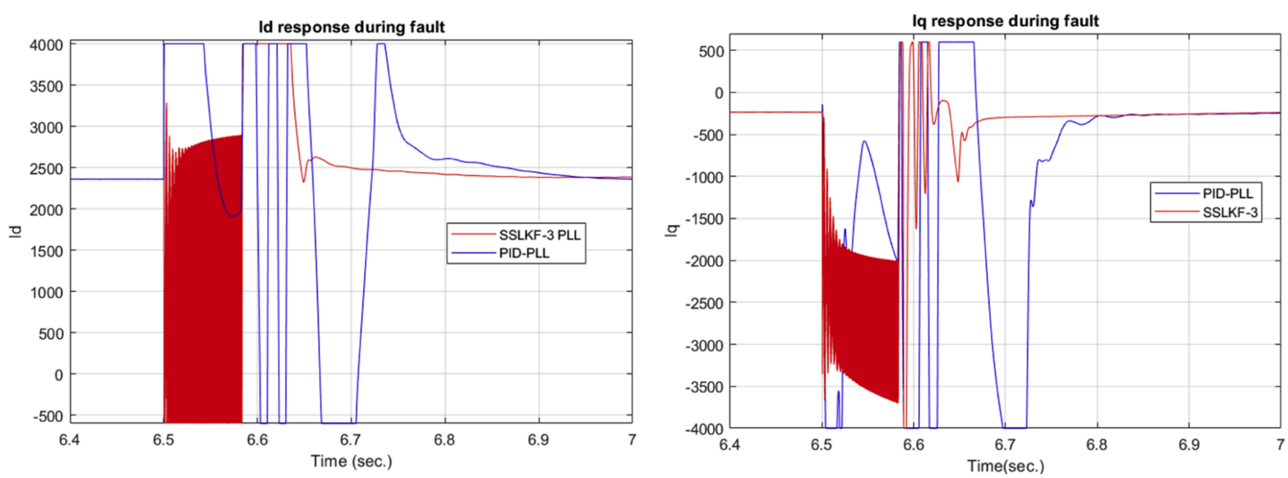

Fig. 8. Current responses of GFLI inverter against 3-phase symmetrical fault.

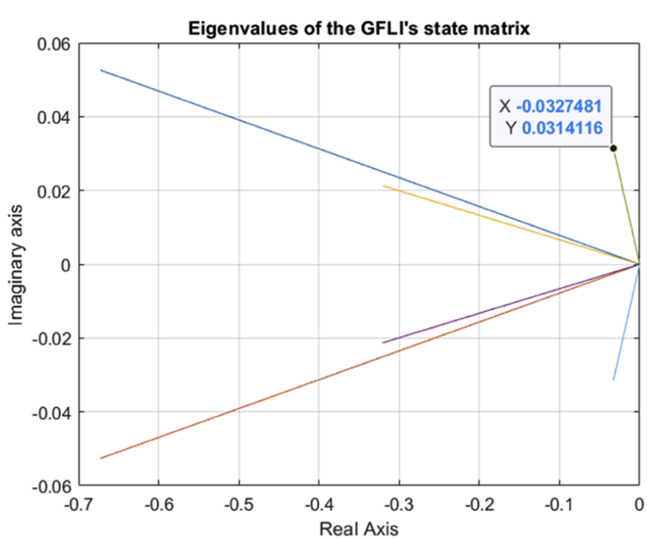

Fig. 9. Eigen values of the GFLI inverter's state matrix.

of X/R, the system becomes unstable. However, this instability can be mitigated by a virtual impedance interface in the control loop, as evaluated in the dedicated subsection below. Fig. 14 (b) to (e) show the importance of maintaining high X/R ratio to have transient stability. Network impedance angle has a significant impact on transient stability. Active and reactive power flows are no longer separated at low X/R ratios because the real part of the line impedance is non-negligible. A real power change brought on by a fault causes a voltage magnitude disturbance, which in turn disturbs the active power balance. The system becomes unstable at low X/R levels because of this positive feedback route, which is lacking in high X/R networks. Even in situations where the physical network does not offer adequate inductive isolation, the virtual impedance control that has been suggested as a cure effectively decouples the P–Q interactions in the control domain by artificially inflating the apparent X/R ratio observed at the GFMI output terminal.

GFMI and strong grid. In this scenario, a 200 MVA SM with an inertia of 5 s. is put into parallel operation with a 2.5 MVA GFMI. When they run individually, SM has a 50 Hz. Constant frequency whereas the GFMI oscillates between 50.0007 and 49.999 Hz. The SM is loaded with 150 MW and 20 MVAR load while the GFMI is loaded with 2 MW and 0.2

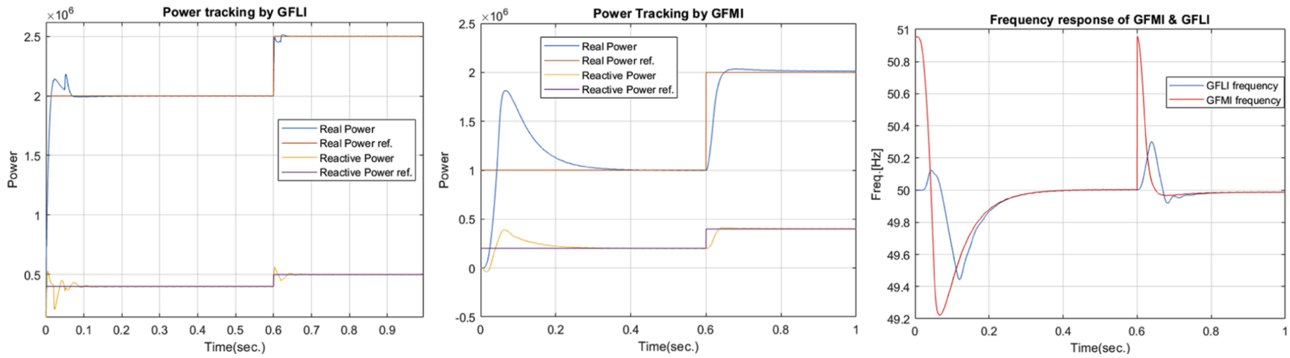

Fig. 10. GFLI and GFMI response in a 100% RES system.

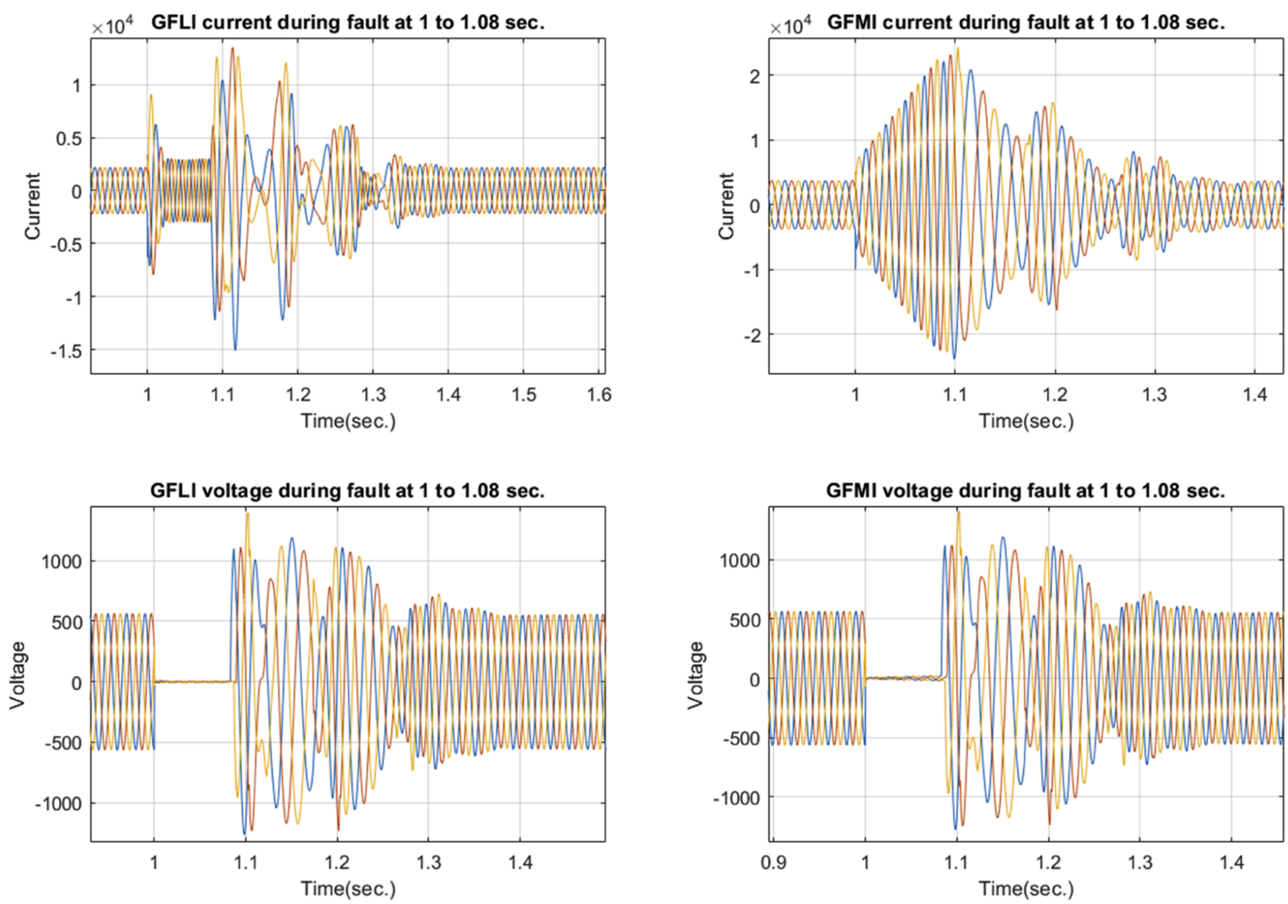

Fig. 11. Fault voltage and current of GFMI, GFLI with PID-PLL.

MVAR. At 0.85 s., they are thrown to synchronism as indicated in Fig. 15.

To check the transient stability, a three-phase bolted symmetrical fault is introduced at 1.8 s. The voltage abruptly spikes to 200% after fault clearing and remains elevated for approximately ten cycles. The response of the GFMI is shown in Fig. 16. Since the GFMI has very little equivalent inertia, it experiences a large frequency sag with a RoCoF of approximately 1 Hz/0.1 s. In contrast, the SM frequency response shows only a small deviation because of its much larger inertia, and therefore it scarcely moves during or after the fault. Fig. 17(a) shows the SM response during the fault, where the low rate of change is consistent with the heavy inertia observed in Fig. 16(d). Fig. 17(b) further illustrates the coupled frequency interaction during and after the fault, noting that the fault is applied at 1.5 s instead of 1.8 s in this case.

At a low X/R ratio, for example X/R = 0.8, the frequency interaction becomes unstable, and the GFMI and SM are unable to converge to a common bus frequency, resulting in loss of synchronism. This behaviour is consistent with the equal-area criterion: at low X/R, the maximum synchronizing power transferable between the GFMI and SM is reduced; consequently, the rotor-angle separation increases, and the kinetic energy injected during the fault exceeds the available decelerating area. This finding highlights the inherent stability limitation of GFMI–SM interconnection through resistive networks under uncompensated operation. In particular, the instability cannot be overcome by virtual inertia tuning alone, since virtual inertia does not directly restore the active–reactive power decoupling lost at low X/R ratios. Therefore, maintaining sufficient synchronizing torque requires either network reinforcement or an additional compensation mechanism, such as

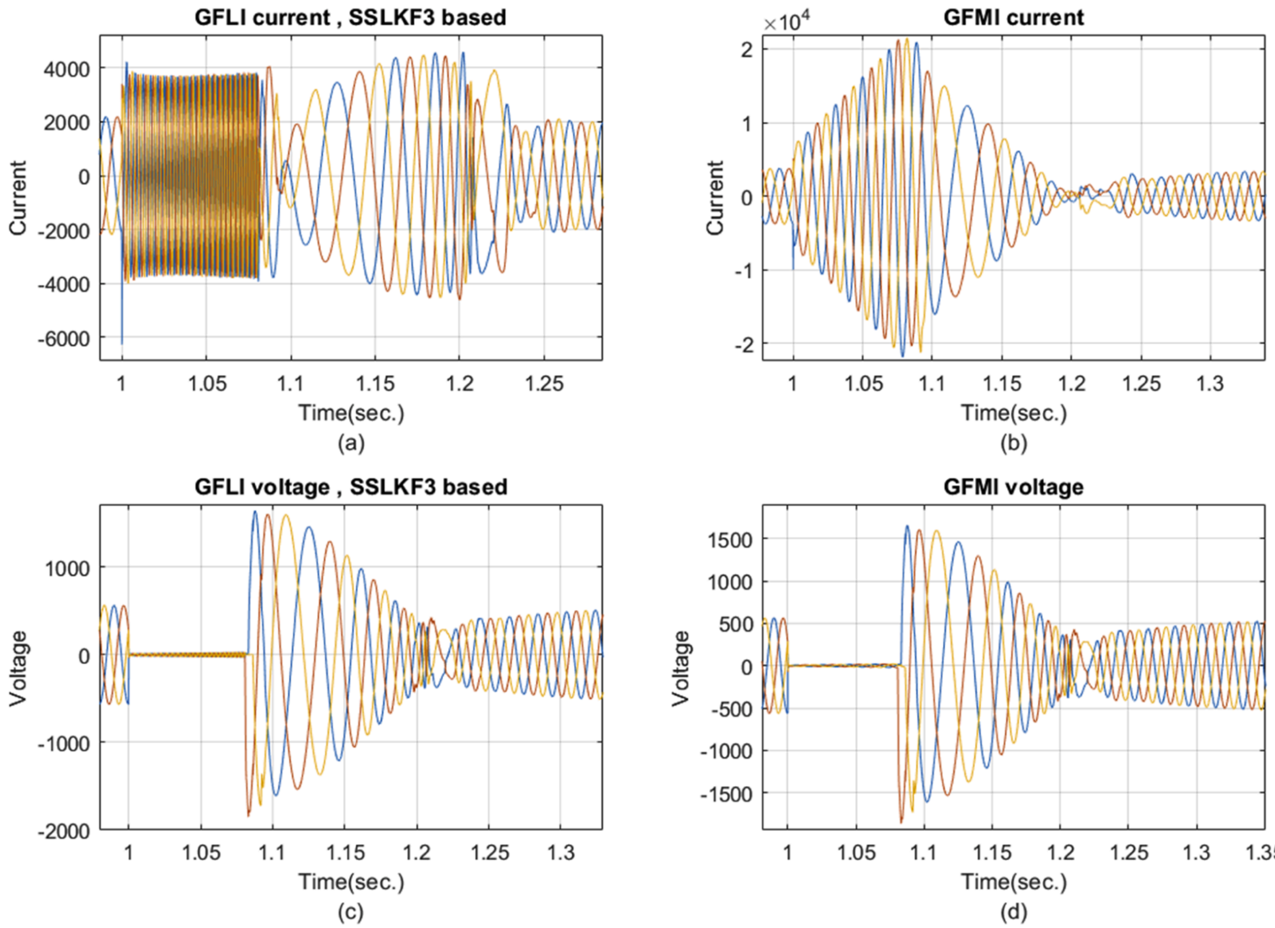

Fig. 12. Fault voltage and current of GFMI, GFLI with SSLKF3-PLL.

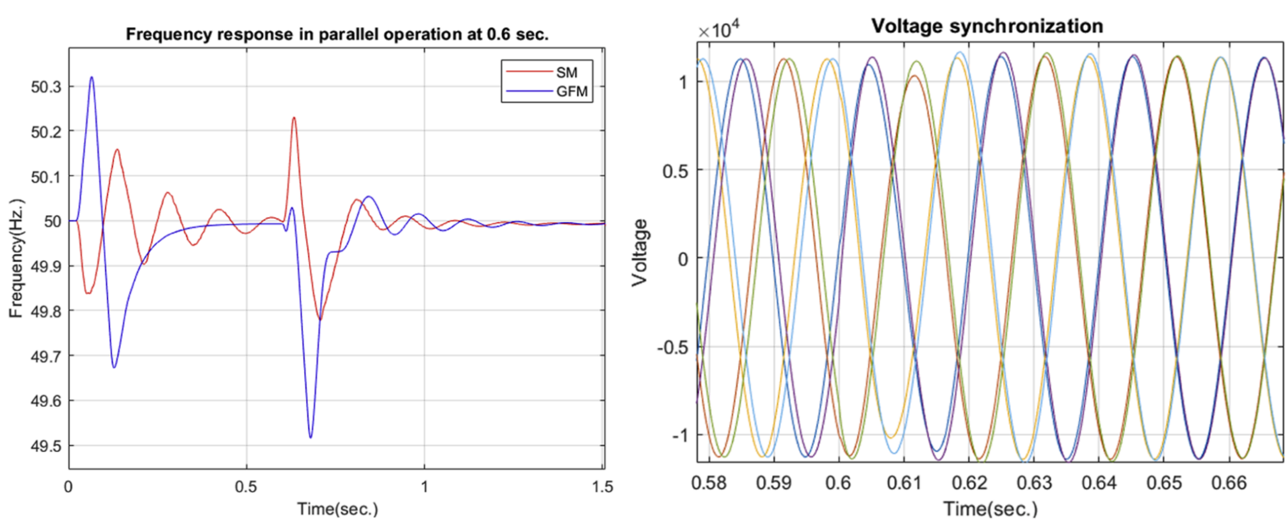

Fig. 13. Frequency and Voltage in parallel operation.

virtual impedance. The instability discussed here is observed before introducing virtual impedance compensation; the following subsection therefore evaluates whether a fixed virtual reactance can recover synchronism under the same low-X/R conditions.

The state matrix of GFMI is analyzed which is a 10 × 10 matrix. Eigenvalues of the matrix is plotted as shown in Fig. 18. The critical Eigenvalue is -.032±031i, which has a damping ratio of 0.72. It clearly indicates that the GFMI system is stable against disturbances at a certain level.

VI loop in low X/R ratio of both weak and strong grid. At X/R = 0.8, both weak- and strong-grid GFMI–SM systems lose stability. To reassess the stability margin, virtual impedance (VI) compensation is introduced. A constant virtual reactance of $X_v = 5\,\Omega$(approximately 5% of the base impedance) is added to the GFMI voltage-control loop. By modifying the

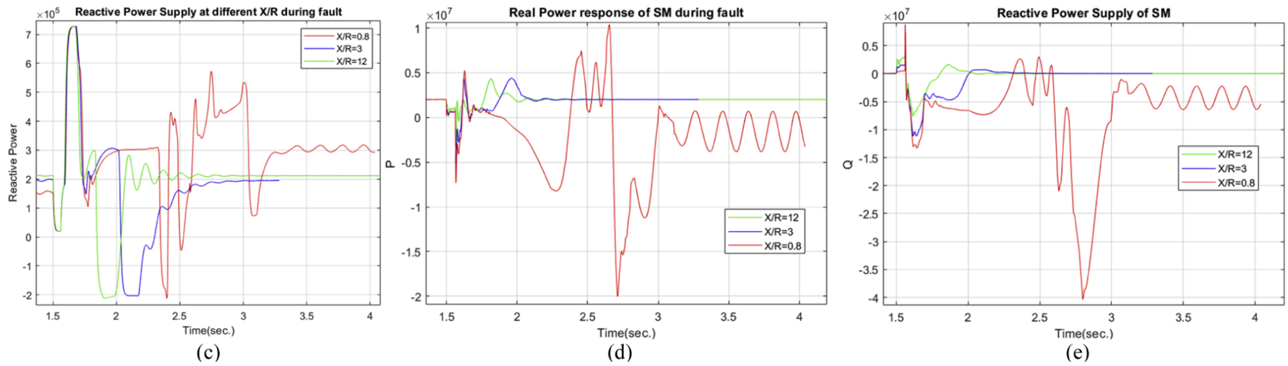

Fig. 14. Impact of X/R ratio on GFMI and SM responses.

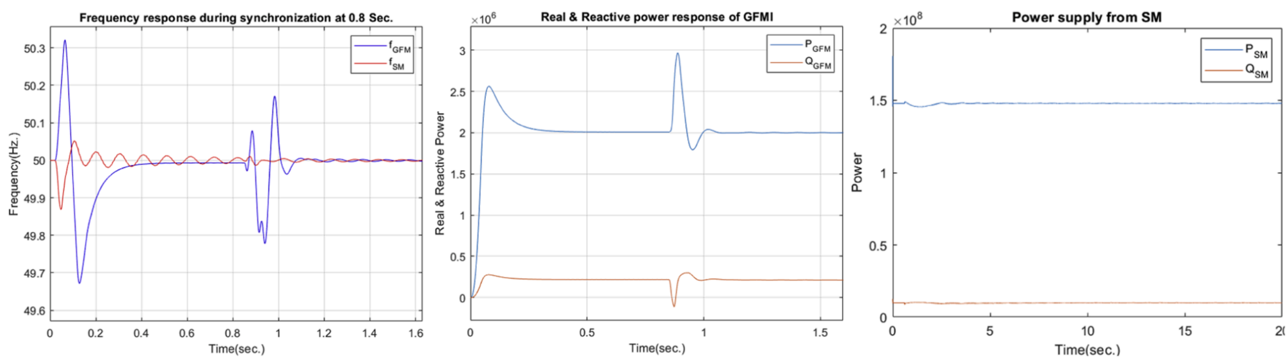

Fig. 15. GFMI and Strong SM steady state outputs.

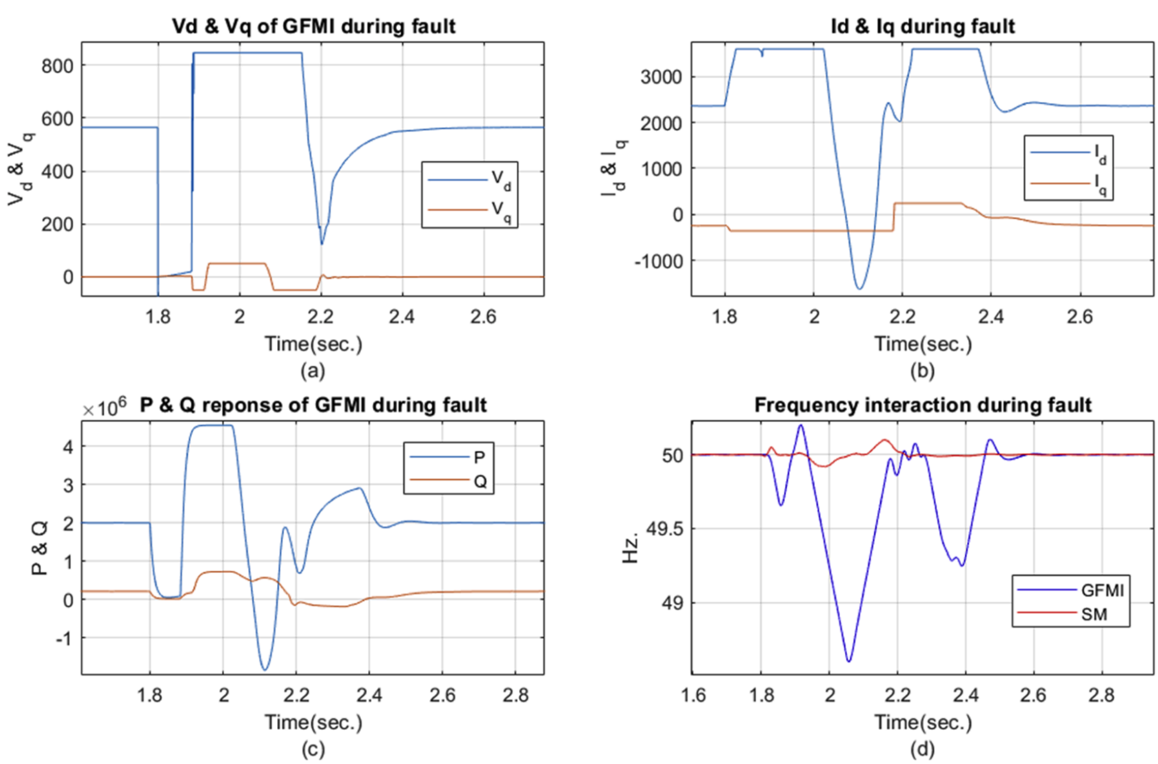

Fig. 16. Voltage, power, frequency response during fault.

converter terminal voltage according to the measured output current, the controller effectively increases the apparent X/R ratio without changing the physical network. This enhancement improves active–reactive power decoupling at the point of interconnection, strengthens synchronizing power transfer between the GFMI and SM, and enlarges the decelerating area predicted by the equal-area criterion.

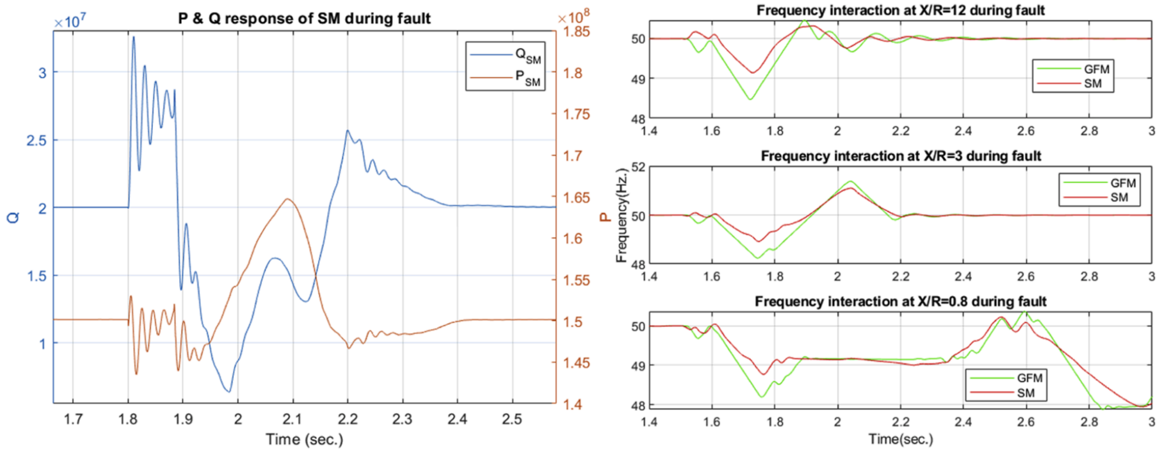

Fig. 17. (a) Response of SM during fault (b) Frequency response.

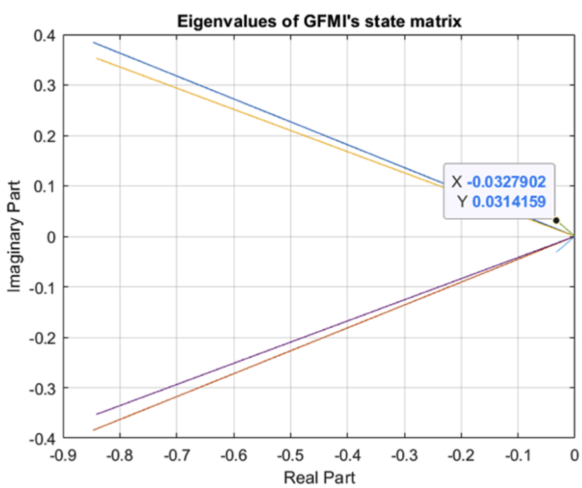

Fig. 18. Eigenvalues of GFMI's state matrix.

For the weak-grid scenario (2 MVA SM, $H = 1.5$s; Fig. 19), VI progressively recovers stability down to X/R = 0.56. However, stability is again lost at X/R = 0.55, marking the limit of effectiveness for the fixed compensation. The reason is that the added virtual reactance compensates only the reactive component of voltage–current coupling, whereas the resistive component remains unchanged. As X/R decreases, the influence of resistance becomes increasingly dominant, eventually overwhelming the gain in synchronizing power provided by the VI and allowing the intrinsic P–V feedback instability to re-emerge. Consequently, X/R = 0.55 defines the critical ratio for this operating condition.

A substantially different response is observed in Fig. 20 for the strong-grid case with a 200 MVA SM ($H = 4.5$ s). Here, VI preserves stable operation across the entire range and maintains synchronism even at X/R = 0. The key factor is the greatly increased kinetic energy stored in the larger machine—roughly 300 times greater than that of the 2 MVA SM. As a result, the machine behaves almost like an infinite bus, significantly reducing bus-voltage disturbances and enabling the same fixed virtual reactance to provide sufficient synchronization support even when the physical network contains no reactance.

12. Conclusion

This paper investigates several prospective scenarios of future power systems involving GFLI, GFMI, and SM-based grids. It first examines GFLI, which is presently the most widely adopted inverter type in power systems. As synchronous machines are progressively replaced by inverter-based resources, the grid becomes weaker, and conventional GFLI control faces stability challenges because its PLL becomes more

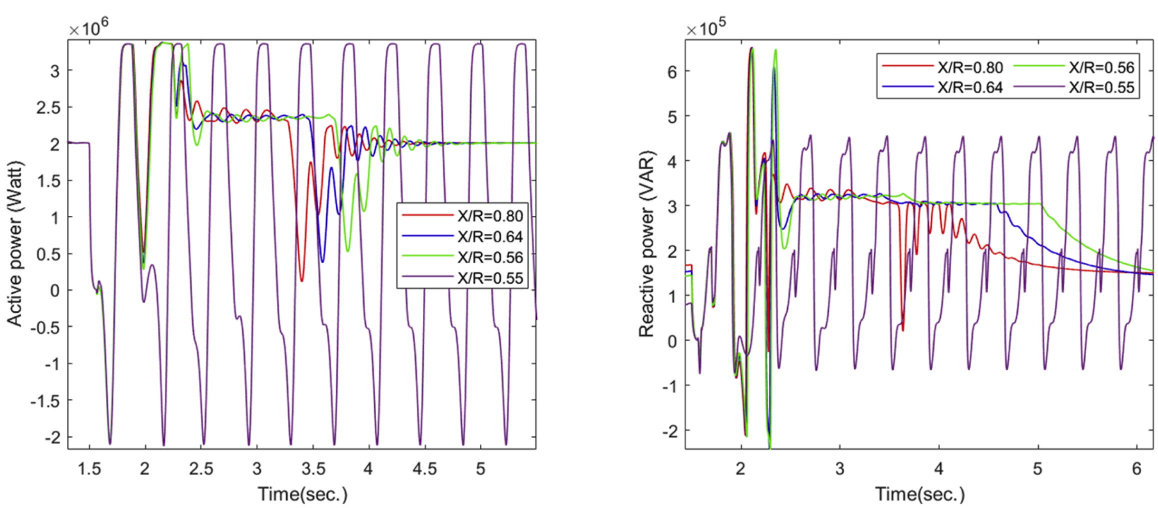

Fig. 19. Weak SM and GFMI power response with VI loop in low X/R ratios.

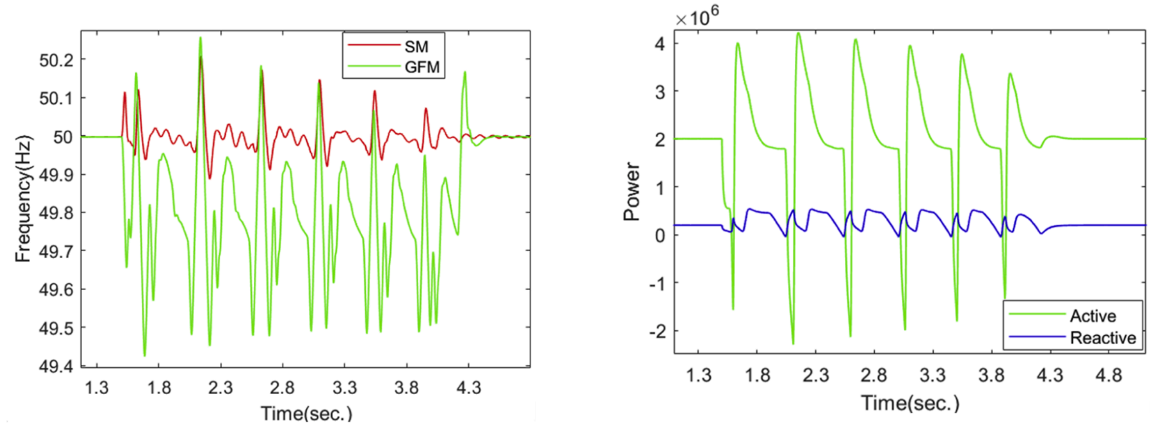

(a) (b)

Fig. 20. Strong SM and GFMI with VI loop at X/R = 0: (a) Frequency response (b) Power response.

sensitive to weak-grid voltage and angle variations. To address this issue, a Kalman-filter-based SSLKF-3 PLL is adopted and evaluated within the considered system scenarios. The results demonstrate stable operation within the studied conditions and show that SSLKF-3 improves the GFLI response compared with a conventional PID-based PLL, particularly by reducing short-circuit current, limiting current stress, and shortening settling time after large disturbances.

Secondly, toward a 100% renewable-energy-based power system, the interaction between GFLI equipped with SSLKF-3-PLL and GFMI is investigated under both steady-state and transient conditions. Within the studied operating point and fault conditions, the GFLI–GFMI system remains stable, and the SSLKF-3-PLL reduces fault-current contribution and disturbance stress on the GFMI. These results indicate that GFLI–GFMI coordination can support fully inverter-interfaced operation, although the conclusion is limited to the tested ratings, controller parameters, and disturbance cases.

This paper further investigates the parallel operation of GFMI with SM-based grids under weak- and strong-grid conditions. The results show that transient stability is strongly influenced by the network X/R ratio rather than by grid-strength classification alone. Without compensation, instability occurs below X/R = 0.8 in both weak- and strong-grid interconnections. Virtual impedance compensation is then introduced as a control-loop modification to improve low-X/R stability. For the weak-grid case with a 2 MVA SM and $H = 1.5$s, it restores stability down to X/R = 0.55, below which resistive coupling dominates. For the strong-grid case with a 200 MVA SM and $H = 4.5$s, the same compensation maintains synchronism even at X/R = 0 due to the much larger stored kinetic energy of the SM. Therefore, virtual impedance is shown to be effective but bounded, with its performance depending jointly on network impedance, machine inertia, control settings, and disturbance severity. Eigenvalue analysis of the linearized GFLI and GFMI state-space models further supports the observed time-domain stability trends within the studied parameter range.

Some future extension of this present work will involve local measurement-based indicator which can provide PLL information much earlier independent of being predictor-corrector steps. Also, hardware in loop (HIL) based validation and larger system will be investigated.

- Availability of data and material: Based on request, data will be made available.
- Competing interests: There is no conflict of interest.
- Funding: Authors received no funding.
- Authors' contributions: First author have done all the works from top to bottom, second and third author supervises the work and has guided the work, fourth author helps in writing.
- Acknowledgements: This is an original research paper.

Data availability

Data is available if needed.

Declaration of generative AI and AI-assisted technologies in the manuscript preparation process

During the preparation of this work the author(s) used 1- chat.figures.ai; to generate figure 2 and figure 5. After using this tool/service, the author(s) reviewed and edited the content as needed and take(s) full responsibility for the content of the published article.

CRediT authorship contribution statement

Pollen Barua: Writing – review & editing, Writing – original draft, Visualization, Validation, Software, Resources, Project administration, Methodology, Investigation, Formal analysis, Data curation, Conceptualization. **Evert Agneholm:** Supervision. **Yaksh Kumar:** Writing – review & editing. **Naime Ahmadi:** Writing – review & editing, Investigation. **Kjetil Obstfelder Uhlen:** Writing – review & editing, Visualization, Supervision, Project administration, Investigation, Formal analysis, Conceptualization.

Declaration of interest

There is no conflict of interest in the work.

Appendix: Simulation system parameters

The MATLAB/Simulink-based simulation platform is configured at a fixed time step of $T_{step} = 20$us.

A.1. Grid base parameters

The grid is modelled as a 50 Hz, 2 MVA, 13.8 kV (line-to-line RMS) three-phase system. All per-unit base quantities are computed as follows:

Parameter	Symbol	Expression	Value	Unit
Nominal frequency	f	—	50	Hz
Angular frequency	ω	$2\pi f$	314.16	rad/s
Apparent power base	S_b	—	2.0	MVA
Voltage base (L-L RMS)	V_b	—	13.8	kV
Phase peak voltage	$V_{ph,pk}$	$V_b\sqrt{2/3}$	11,267.65	V
Current base (RMS)	I_b	$S_b/(\sqrt{3}\,V_b)$	83.67	A
Current base (peak)	$\hat{I}_b$	$\sqrt{2}I_b$	118.33	A
Impedance base	Z_b	V_b^2/S_b	95.22	Ω
Inductance base	L_b	Z_b/ω	303.09	mH
Capacitance base	C_b	$(Z_b\omega)^{-1}$	33.43	μF

A.2. Grid source impedance

The grid source impedance is determined by the short circuit ratio (SCR) and X/R ratio:

Parameter	Symbol	Expression	Value	Unit
Short circuit ratio	SCR	—	10	—
X/R ratio	X/R	—	7	—
Source impedance (p.u.)	Z_{pu}	1/SCR	0.1	p.u.
R/Z ratio	—	$1/\sqrt{1+(X/R)^2}$	0.14,142	—
X/Z ratio	—	$(X/R)\cdot(R/Z)$	0.98,995	—
Source resistance (p.u.)	R_{pu}	$Z_{pu}\cdot(R/Z)$	0.014,142	p.u.
Source reactance (p.u.)	X_{pu}	$Z_{pu}\cdot(X/Z)$	0.098,995	p.u.
Source inductance	L_{source}	$X_{pu}\cdot L_b$	30.00	mH
Source resistance	R_{source}	$R_{pu}\cdot Z_b$	1.347	Ω

A.3. Transformer

The step-down transformer interfaces the 13.8 kV grid to the inverter low-voltage bus:

Parameter	Symbol	Value	Unit
Primary voltage	V_{prim}	13,800	V
Secondary voltage	V_{sec}	397.72	V
Transformer rating	S_{trf}	5	MVA

A.4. VSC base parameters

The voltage source converter operates from a 1250 V DC bus. VSC base quantities are derived independently from the grid base:

Parameter	Symbol	Expression	Value	Unit
Switching frequency	f_{sw}	—	10,000	Hz
DC link voltage	V_{dc}	—	1250	V
AC phase peak voltage	$\hat{V}_{ph}$	$V_{dc}/2$	625.0	V
VSC voltage base	$V_{b,VSC}$	$0.7\hat{V}_{ph}\sqrt{3}/\sqrt{2}$	535.83	V
VSC power base	$S_{b,VSC}$	—	2.0	MVA
VSC current base (RMS)	$I_{b,VSC}$	$S_{b,VSC}/(\sqrt{3}\,V_{b,VSC})$	2154.99	A
VSC current base (peak)	$\hat{I}_{b,VSC}$	$\sqrt{2}I_{b,VSC}$	3047.62	A
VSC impedance base	$Z_{b,VSC}$	$V_{b,VSC}^2/S_{b,VSC}$	0.14,355	Ω
VSC inductance base	$L_{b,VSC}$	$Z_{b,VSC}/\omega$	0.4569	mH
VSC capacitance base	$C_{b,VSC}$	$(Z_{b,VSC}\omega)^{-1}$	22.17	mF

A.5. LCL filter parameters

The LCL output filter is designed to attenuate switching harmonics. $L_1$is sized to limit peak-to-peak current ripple to 15% of the rated peak current. $L_2$is determined from the desired attenuation factor $k_a = 0.2$at the switching frequency:

Parameter	Symbol	Value	Unit
Inverter-side inductance	L_1	45.57	μH
Filter capacitance	C_f	2217.34	μF
Attenuation factor	k_a	0.2	—
Grid-side inductance	L_2	0.685	μH
Damping resistance	R_f	2.153	mΩ
L_1/L_2ratio	—	66.49	—
LCL resonance frequency	f_{res}	4113.07	Hz

The resonance frequency $f_{res} = 4113\text{Hz}$ falls between the fundamental (50 Hz) and the switching frequency (10 kHz), satisfying the standard LCL design criterion $10f \le f_{res} \le f_{sw}/2$.

A.6. Inner current controller (GFL and GFM)

The current controller is a PI regulator tuned to achieve a closed-loop bandwidth of 1 kHz:

Parameter	Symbol	Value	Unit
Proportional gain	$K_{p,c}$	5	—
Integral gain	$K_{i,c}$	5000	—
Control bandwidth	f_c	1000	Hz
Time constant	t_c	1.0	ms

A.7. GFM voltage and current controller parameters

Parameter	Symbol	Value	Unit
Damping factor	ζ	1.1	—
Voltage loop bandwidth	$\omega_v = 2\pi(f_{sw}/100)$	628.32	rad/s
Voltage loop proportional gain	$K_{p,v}$	3.065	—
Voltage loop integral gain	$K_{i,v}$	875.37	—
Current loop proportional gain	$K_{p,i}$	0.06,084	Ω
Current loop integral gain	$K_{i,i}$	179,914.66	—

A.8. SSLKF-3 PLL parameters

Parameter	Symbol	Value	Unit
Sampling period	T_s	0.0001	s
Angle correction gain	K_1	0.9	—
Frequency correction gain	K_2	10	—
Acceleration correction gain	K_3	150	—

References

[1] U.S. Energy Information Administration (EIA), International Energy Outlook 2019: With Projections to 2050. Washington, DC, USA: U.S. Department of Energy, Office of Energy Analysis, Sep. 2019. Available: https://www.eia.gov/outlooks/ieo/pdf/ieo2019.pdf.

[2] S. Brown and D. Jones, European Electricity Review 2024: Europe's Electricity Transition Takes Crucial Strides Forward. London, U.K.: Ember, Feb. 2024. Available: https://ember-energy.org/latest-insights/european-electricity-review-2024/.

[3] O. Homaee, S. Jadid, Investigation of synchronous generator in reactive power market: An accurate view, IET Gen., Transm. Distribut. 8 (11) (2014) 1881–1890, https://doi.org/10.1049/iet-gtd.2013.0901.

[4] P.M. Anderson, V. Vittal, J.D. McCalley, A.A. Fouad. Power System Control and Stability, 3rd ed., Wiley-IEEE Press, Hoboken, NJ, USA, 2019.

[5] P. Barua, V. Shekher, V. Kumar, M.F. Ansari, A.C. Alguno, R. Barua, Rotor angle stability and voltage stability improvement of highly renewable energy penetrated western grid of Bangladesh power system using FACTS device, Cogent Eng. 10 (1) (2023) 2210899, https://doi.org/10.1080/23311916.2023.2210899.

[6] P. Kundur. Power System Stability and Control, McGraw-Hill, New York, NY, USA, 1994.

[7] B. Kroposki, "Summarizing the Technical Challenges of High Levels of Inverter-Based Resources in Power Grids," National Renewable Energy Laboratory (NREL), Golden, CO, USA, Rep. NREL/PR-5D00-73869, Apr. 2019. [Online]. Available: https://www.nrel.gov/docs/fy19osti/73869.pdf.

[8] P. Barua, R. Barua, V. Shekher, M. Quamruzzaman, M.G. Rabbani, Q. Ai, Contingency analysis and adoption of STATCOM in highly renewable energy penetrated Western Grid of Bangladesh, Cogent Eng. 9 (1) (2022) 2076550, https://doi.org/10.1080/23311916.2022.2076550.

[9] P. Barua, R. Barua, Machine learning based solar energy forecasting and wind-solar based hybrid grid arrangement at Patenga coastal area, Bangladesh, in: In: 2021 IEEE International Conference on Power, Electrical, Electronic and Industrial Applications (PEEIACON), Dhaka, Bangladesh, 2021, pp. 53–57. https://doi.org/10.1109/PEEIACON54708.2021.9929754.

[10] P. Barua, M.G. Rabbani, M. Quamruzzaman, Impact of Wind Power plant in Bangladesh power system stability, in: In: 2021 3rd International Conference on Sustainable Technologies for Industry 4.0 (STI), Dhaka, Bangladesh, 2021, pp. 1–5. https://doi.org/10.1109/STI53101.2021.9732614.

[11] P. Barua, R. Barua, M. Quamruzzaman, M.G. Rabbani, Influence of large scale solar power on stability of East West Interconnector System of Bangladesh power system, in: in 2021 5th International Conference on Electrical Engineering and Information Communication Technology (ICEEICT), Dhaka, Bangladesh, 2021, pp. 1–4. https://doi.org/10.1109/ICEEICT53905.2021.9667859.

[12] Energy Systems Integration Group (ESIG), Toward 100% Renewable Energy Pathways: Key Research Needs. Reston, VA, USA: ESIG, 2019 . Available: https://www.esig.energy/reports-briefs/.
[13] S. Impram, Secil Varbak Nese, Bülent Oral, challenges of renewable energy penetration on power system flexibility: a survey, Energy Strategy Rev. 31 (2020) 100539, https://doi.org/10.1016/j.esr.2020.100539.
[14] X. Gao, D. Zhou, A. Anvari-Moghaddam, F. Blaabjerg, Grid-following and Grid-forming control in power electronic based power systems: A comparative study, in: in IECON 2021 – 47th Annual Conference of the IEEE Industrial Electronics Society, Toronto, ON, Canada, 2021, pp. 1–6. https://doi.org/10.1109/IECON48115.2021.9589432.
[15] H. Zhang, W. Xiang, W. Lin, J. Wen, Grid forming converters in renewable energy sources dominated power Grid: control strategy, stability, application, and challenges, J. Mod. Power Syst. Clean Energy 9 (6) (2021) 1239–1256, https://doi.org/10.35833/MPCE.2021.000257.
[16] H. Ahmed, S. Biricik, M. Benbouzid, Linear Kalman filter-based grid synchronization technique: an alternative implementation, IEEE Trans. Ind. Inform. 17 (6) (2021) 3847–3856, https://doi.org/10.1109/TII.2020.3009032.
[17] E. Ebinyu, O. Abdel-Rahim, D.-E.A. Mansour, M. Shoyama, S.M. Abdelkader, Grid-forming control: advancements towards 100% inverter-based grids—A review, Energies 16 (2023) 7579, https://doi.org/10.3390/en16227579.
[18] Z. Li, C. Zang, P. Zeng, H. Yu, S. Li, J. Bian, Control of a grid-forming inverter based on sliding-mode and mixed H2/H∞ Control, IEEE Trans. Ind. Electron. 64 (2017) 3862–3872.
[19] C. Ai, Y. Li, J. Liu, A strong-grid-friendly voltage control method of grid-forming inverters, in: in 2023 IEEE 2nd International Power Electronics and Application Symposium (PEAS), Guangzhou, China, 2023, pp. 785–790. https://doi.org/10.1109/PEAS58692.2023.10395073.
[20] R. Lliuyacc, J.M. Mauricio, A. Gomez-Exposito, M. Savaghebi, J.M. Guerrero, Grid-forming VSC control in four-wire systems with unbalanced nonlinear loads, Electr. Power Syst. Res. 152 (2017) 249–256.
[21] R. Lasseter, Z. Chen, D. Pattabiraman, Grid-forming inverters: a critical asset for the power Grid, IEEE J. Emerg. Sel. Top. Power Electron. 8 (2019) 925–935.
[22] D. Pattabiraman, R.H. Lasseter, T.M. Jahns, Comparison of grid following and grid forming control for a high inverter penetration power system, in: Proceedings of the 2018 IEEE Power Energy Society General Meeting (PESGM), Portland, OR, USA, 2018, pp. 1–5.
[23] F. Zhao, et al., Control interaction modeling and analysis of grid-forming battery energy storage system for offshore Wind Power plant, IEEE Trans. Power Syst. 37 (1) (2022) 497–507, https://doi.org/10.1109/TPWRS.2021.3096850.
[24] H. Pishbahar, F. Blaabjerg, H. Saboori, Emerging grid-forming power converters for renewable energy and storage resources integration – A review, Sustain. Energy Technol. Assess. 60 (2023) 103538, https://doi.org/10.1016/j.seta.2023.103538.
[25] S. Shahzad, M.A. Abbasi, H. Ali, M. Iqbal, R. Munir, H. Kilic, Possibilities, challenges, and future opportunities of microgrids: a review, Sustainability 15 (2023) 6366, https://doi.org/10.3390/su15086366.
[26] D.B. Rathnayake, M. Akrami, C. Phurailatpam, S.P. Me, S. Hadavi, G. Jayasinghe, S. Zabihi, B. Bahrani, Grid forming inverter modeling, control, and applications, IEEE Access 9 (2021) 114781–114807.
[27] N. Mohammed, H. Udawatte, W. Zhou, D.J. Hill, B. Bahrani, Grid-forming inverters: a comparative study of different control strategies in frequency and time domains, IEEE Open J. Ind. Electron. Soc. 5 (2024) 185–214, https://doi.org/10.1109/OJIES.2024.3371985.
[28] J.A. Suul, S. D'Arco, P. Rodriguez, M. Molinas, Impedance compensated grid synchronization for extending the stability range of weak grids with voltage source converters, IET Gener. Transm. Distrib. 10 (6) (2016) 1315–1326.
[29] Y. Li, Y. Gu, Y. Zhu, A. Junyent-Ferré, X. Xiang, T.C. Green, Impedance circuit model of grid-forming inverter: visualizing control algorithms as circuit elements, IEEE Trans. Power Electron. 36 (3) (2021) 3377–3395.
[30] Z. Tao, D. Dezhi, An improved IPT-PLL technology for single-phase grid-connected inverters in complex power grid conditions, Sci. Rep. 14 (2024) 12169, https://doi.org/10.1038/s41598-024-62702-y.
[31] C. Zhang, X. Wang, F. Blaabjerg, W. Wang, C. Liu, The influence of phase-locked loop on the stability of single-phase grid-connected inverter, in: In: 2015 IEEE Energy Conversion Congress and Exposition (ECCE), 2015, pp. 4737–4744.
[32] A.A.A. Radwan, Y.A.-R.I. Mohamed, Power synchronization control for grid connected current-source inverter-based photovoltaic systems, IEEE Trans. Energy Convers. 31 (3) (2016) 1023–1036.
[33] T.A. Taha, M. Shalaby, N.I.A. Wahab, H.I. Zaynal, M.K. Hassan, S. Al-Sowayan, M. A. Alawad, Recent advancements in multilevel inverters: topologies, modulation techniques, and emerging applications, Symmetry 17 (2025) 1010, https://doi.org/10.3390/sym17071010.
[34] O.A. Storlien, Comparison of Droop-Based Grid-Forming and PLL-Based Grid-Following Control of VSC During Symmetrical Fault. Master's thesisDept. Elect. Power Eng., Norwegian University of Science and Technology (NTNU), 2022.
[35] S. Golestan, J.M. Guerrero, J.C. Vasquez, Three-phase PLLs: a review of recent advances, IEEE Trans. Power Electron. 32 (3) (2017) 1894–1907.
[36] A. Bellini, et al., A robust synchronization method for centralized microgrids, IEEE Trans. Ind. Appl. 51 (2015) 1602–1609.
[37] S. Golestan, J.M. Guerrero, J.C. Vasquez, Steady-State linear kalman filter-based PLLs for power applications: a second look, IEEE Trans. Ind. Electron. 65 (12) (2018) 9795–9800, https://doi.org/10.1109/TIE.2018.2823668.
[38] S.B. Bellini, V. Iacovone, Robust PLL algorithm for three-phase grid-connected converters, EPE J. 20 (4) (2010) 22–30.
[39] C.K. Chui, G. Chen. Kalman Filtering: With Real-Time Applications, 5th ed., Springer, Heidelberg, Germany, 2017 https://doi.org/10.1007/978-3-319-47612-4.
[40] M. Nichol. System Rate of Change of Frequency: A GHD Survey of International Views, GHD Pty Ltd., Tech. Rep, Australia, 2022.
[41] N. Modi, R. Yan, et al., Low inertia power systems: Frequency response challenges and a possible solution, in: 2016 Australasian Universities Power Engineering Conference (AUPEC), 2016, pp. 1–6.
[42] L.A.L. Tenorio, "Hydro Turbine and Governor Modelling, Electric-Hydraulic Interaction. M.S. thesis, Dept. Electric Power Eng., Norwegian University of Science and Technology (NTNU), Trondheim, Norway, 2010.